A Novel 2D Graphene Oxide Modified α-AgVO3 Nanorods: Design, Fabrication and Enhanced Visible-Light Photocatalytic Performance

Yan Xing (xingyan618@njupt.edu.cn)
Nanjing University of Posts and Telecommunications https://orcid.org/0000-0002-7210-2458
Jian WU
Nanjing University of Posts and Telecommunications
Xin MIN
China University of Geosciences Beijing
Xingao LI
Nanjing University of Posts and Telecommunications

Research Article

Keywords: α-AgVO3, GO/α-AgVO3, Photocatalysis, GO nanosheets, In-suit coprecipitation processing

Posted Date: June 3rd, 2021

DOI: https://doi.org/10.21203/rs.3.rs-577266/v1

Title Page

A novel 2D graphene oxide modified α-$AgVO_3$ nanorods: Design, fabrication and enhanced visible-light photocatalytic performance

Jian WU [a], Yan XING [a*], Xin MIN [b], Xingao LI [a*]

[a] New Energy Technology Engineering Lab of Jiangsu Province, School of Science, Nanjing University of Posts & Telecommunications (NUPT), Nanjing 210023, China

[b] Beijing Key Laboratory of Materials Utilization of Nonmetallic Minerals and Solid Wastes, National Laboratory of Mineral Materials, School of Materials Science and Technology, China University of Geosciences (Beijing), Beijing 100083, China

Corresponding authors:

Dr. Yan Xing, E-mail: xingyan618@njupt.edu.cn

Dr. Xing'ao Li, E-mail: lixa@njupt.edu.cn

Abstract

Silver vanadates are promising visible-light-responded photocatalysts with suitable bandgap for solar absorption. However, the easy recombination of photogenerated carriers limits their performance. To overcome this obstacle, a novel 2D graphene oxide (GO) modified α-$AgVO_3$ nanorods (GO/α-$AgVO_3$) photocatalyst was designed herein to improve the separation of photocarriers. The GO/α-$AgVO_3$ was fabricated through a facile in-suit coprecipitation method at room temperature. It was found that the as-prepared 0.5 wt.% GO/α-$AgVO_3$ exhibited the most excellent performance for Rhodamine B (RhB) decomposition, with an apparent reaction rate constant 18 times higher than that of pure α-$AgVO_3$ under visible-light irradiation. In light of the first-principles calculations and the heterojunction analysis, the mechanism underpinned the enhanced photocatalytic performance was proposed. The enhanced photocatalytic performance was ascribed to the appropriate bandgap of α-$AgVO_3$ nanorods for visible light response and efficient separation of photocarriers through GO nanosheets. This work demonstrates the feasibility of overcoming the easy recombination of photogenerated carriers and provides a valuable GO/α-$AgVO_3$ photocatalyst for pollutant degradation.

Keywords: α-$AgVO_3$; GO/α-$AgVO_3$; Photocatalysis; GO nanosheets; In-suit coprecipitation processing

1. Introduction

The elimination of toxic organic dyes that hazarded to water resources and human health has aroused widespread attentions [1,2]. Photocatalysis has been regarded as a promising approach to surmount these concerns, wherein visible-light-driven photocatalysts play an important role [3,4]. However, currently, there are two limitations that hinder the performance and applications of photocatalysts. One is that the band gap of photocatalyst is not suitable for visible light absorption [5,6], the other is the rapid recombination of photogenerated electrons and holes [7]. To cope with these issues, it is appealing to search for novel photocatalysts with fascinating properties [8,9].

Silver vanadium oxides (SVOs), including $AgVO_3$ [10], $Ag_4V_2O_7$ [11], Ag_3VO_4 [12], and $Ag_2V_4O_{11}$ [13], have been widely exploited in the field of catalysis owing to their excellent electrical properties, controllable surface, and easy availability. Among these SVOs, monoclinic structured α phase $AgVO_3$ is one of the most promising visible-light-responsible photocatalyst because the hybridization of V 3*d*, O 2*p*, and Ag 4*d* orbits can form highly dispersed valence bands with a narrow band gap [14]. For its potential high performance, photocatalytic properties of α-$AgVO_3$ based materials have been explored extensively [15,16]. However, the activity of pristine $AgVO_3$ is still unsatisfactory owing to the fast recombination of photogenerated electrons and holes, which will reduce the photoreaction rate and thus limit its further applications.

Heterojunction construction is an efficient way to overcome the above obstacles. By designing proper heterostructure, including matched band structure and

well-controlled surface, an additional transmission path for the carriers (electrons and holes) can be established at the interface which is helpful to improve the photocatalytic performance. Considering the high chemical stability, large surface area, and high electron mobility, 2D graphene oxide (GO) is regarded as an ideal candidate to act as an electron transmitter [17,18]. For example, enhanced photocatalytic activity has been found in GO/g-C_3N_4/MoS_2 ternary hybrid material, wherein the fast charge transfer pathway through GO plays a key role [19]. Based on these facts, the introduction of GO to build GO/α-$AgVO_3$ nanorods hybrid materials is expected to significantly improve the photocatalytic performance of α-$AgVO_3$.

With this aim, a series of GO/α-$AgVO_3$ photocatalysts were designed in this work and were fabricated by a facial in-suit coprecipitation method. The structure and morphology of the as-prepared GO/α-$AgVO_3$ were systematically characterized. And the photocatalytic performance of GO/α-$AgVO_3$ was evaluated using photodecomposition of RhB as a model reaction. The dynamic of degradative reaction was also analyzed. Moreover, in order to disclose the possible mechanism that underpins the enhanced photocatalytic performance, the band structure of α-$AgVO_3$ was calculated by first-principles calculations based on DFT.

2. Experimental Procedure

2.1. Preparation of α-$AgVO_3$ nanorods and GO/α-$AgVO_3$ photocatalysts

Ammonium metavanadate (NH_4VO_3, ≥ 99%, analytical reagent purchased from Aladdin Chemical Co., Ltd.), silver nitrate ($AgNO_3$, ≥ 99%, analytical reagent) and Rhodamine B (RhB, purchased from Sinopharm Chemical Reagent Co Ltd.), and

Graphene oxide (type SE2430 obtained from the Sixth Elemental Inc.) were used as starting materials. All the reagents were used without further purification.

Pure α-$AgVO_3$ nanorods were fabricated using a coprecipitation method at room temperature. Typically, 1 mmol NH_4VO_3 and 1 mmol $AgNO_3$ were dispersed in 40 mL of deionized water, respectively, and stirred for 1 h to dissolve completely. The $AgNO_3$ solution was added into the NH_4VO_3 solution drop wisely under agitation, then the mixture was stirred continuously for 3h at room temperature. Then α-$AgVO_3$ nanorods were obtained by centrifugation at 6000 r/min for 10 min. The nanorods were washed with distilled water and ethanol for three times and then dried in an oven at 40 °C overnight.

The GO/α-$AgVO_3$ photocatalysts were fabricated by a facial in-situ directly coprecipitation method. Firstly, GO nanosheets (20 mg) were added to deionized water (100 mL), and the suspension was sonicated for 4 h at 10 °C. Likewise, 1 mmol NH_4VO_3 and 1 mmol $AgNO_3$ were prepared separately. The 2D GO nanosheets dispersion with a certain mass fraction ratio (0.5 wt.%, 1.0 wt.%, 2.0 wt.%) was added to NH_4VO_3 solution and stirred for 30 min to reach saturated adsorption of VO_3^- on the surface of GO. Then, the $AgNO_3$ solution was dropped into the mixture slowly, and the mixture was stirred continuously for 3h at room temperature. The as-prepared GO/α-$AgVO_3$ hybrid materials were obtained by centrifugation at 6000 r/min for 10 min. The hybrid materials were washed with distilled water and ethanol three times and then dried in an oven at 40 °C. Briefly, the as-synthesized photocatalysts were

referred as 0.5 GO/α-$AgVO_3$, 1.0 GO/α-$AgVO_3$ and 2.0 GO/α-$AgVO_3$ according to the GO weight percentage, respectively.

2.2. Structural characterization and photocatalytic activity

The phase compositions of the α-$AgVO_3$ and GO/α-$AgVO_3$ were characterized by X-ray diffraction (XRD) on a Bruker D8 diffractometer with Cu Kα radiation (λ=1.5418 Å). The morphology characterizations were conducted on Hitachi S-4800 scanning electron microscope (SEM) with energy dispersive spectroscopy (EDS) for elemental analysis. UV-vis diffuse reflectance spectra (DRS) were carried out on a UV-vis spectrophotometer (UV-3600 PLUS) equipped with an integrating sphere device in the wavelength range of 300-800 nm. Ultraviolet photoelectron spectroscopy (UPS) was characterized with He I (21.22 eV) as the monochromatic light source and the total energy resolution is 100 meV. The X-ray photoelectron spectroscopy (XPS) measurements were measured on ESCALAB 250Xi with an Al Kα source to identify surface chemical composition and chemical states.

The photocatalytic activities of the as-prepared α-$AgVO_3$ and GO/α-$AgVO_3$ were evaluated via the photodegradation efficiency of Rhodamine B (RhB). The experiments were carried out in a photoreactor containing a 300 W Xenon lamp (400 nm cutoff filter) and a circulating cooling water system. For the catalytic experiments, 15 mg of the as-prepared samples were dispersed in 30 ml RhB solution (5 mg/L) and stirred for 30 min in dark to reach the adsorption-desorption equilibrium. Then, the light source was switched on to start the photoreaction, during which, the residual concentration of RhB was monitored by UV–vis absorption spectra at certain time

intervals. The degradation efficiency was calculated from the absorbance of the dye solution at a wavelength of 552 nm.

2.3. Band structure calculation

The band structure of α-$AgVO_3$ was investigated to understand its photocatalytic performance. For this aim, first-principles calculations were conducted using the Cambridge serial total energy package (CASTEP) code [20,21]. The plane-wave basis set cutoff was 760 eV after convergent test. A 2× 2× 3 Monckhorst-Pack *k*-mesh was used to sample the Brillouin zone of α-$AgVO_3$ [22]. Geometry optimization was conducted via the Perdew-Burke-Ernzerhof (PBE) exchange-correlation function within the generalized gradient approximation (GGA) [23]. The convergence tolerance for the total energy and maximum ionic displacement was set as 1.0×10^{-5} eV and 1.0×10^{-3} Å, respectively. After completing the geometry optimization, a OTFG ultrasoft potential and generalized gradient approximation (GGA) functional was used to calculate the band structure of α-$AgVO_3$. To further improve the accuracy of band gap, a hybrid HSE03 exchange-correlation functional was employed which has been proven in obtaining a reliable bandgap for complex oxides [24].

3. Results

3.1. Morphology of α-$AgVO_3$ and GO/α-$AgVO_3$

Fig. 1 shows the morphologies of the α-$AgVO_3$ and GO/α-$AgVO_3$ with various GO weight percentages. As shown in **Fig. 1(a)**, the pure α-$AgVO_3$ sample shows a flower-like morphology, which is composed of plentiful one-dimensional (1D) α-$AgVO_3$ nanorods with a length of 10–15μm and a width of 100–300 nm. **Fig. 1(b-d)**

shows the morphologies of 0.5 GO/α-$AgVO_3$, 1.0 GO/α-$AgVO_3$ and 2.0 GO/α-$AgVO_3$ respectively. The α-$AgVO_3$ nanorods are covered by 2D GO nanosheets, indicating the formation of heterojunctions. Notably, with the increase of GO content, the accumulation of a large amount of lamellar corrugated GO nanosheets can be observed. The composition of GO/α-$AgVO_3$ photocatalyst was further characterized by EDS elemental mapping. As shown in **Fig. 2,** silver, oxygen, and vanadium elements are uniformly distributed on the nanorods, and the corrugated nanosheets correspond to the carbon element, indicating the close coupling of α-$AgVO_3$ nanorods and GO nanosheets.

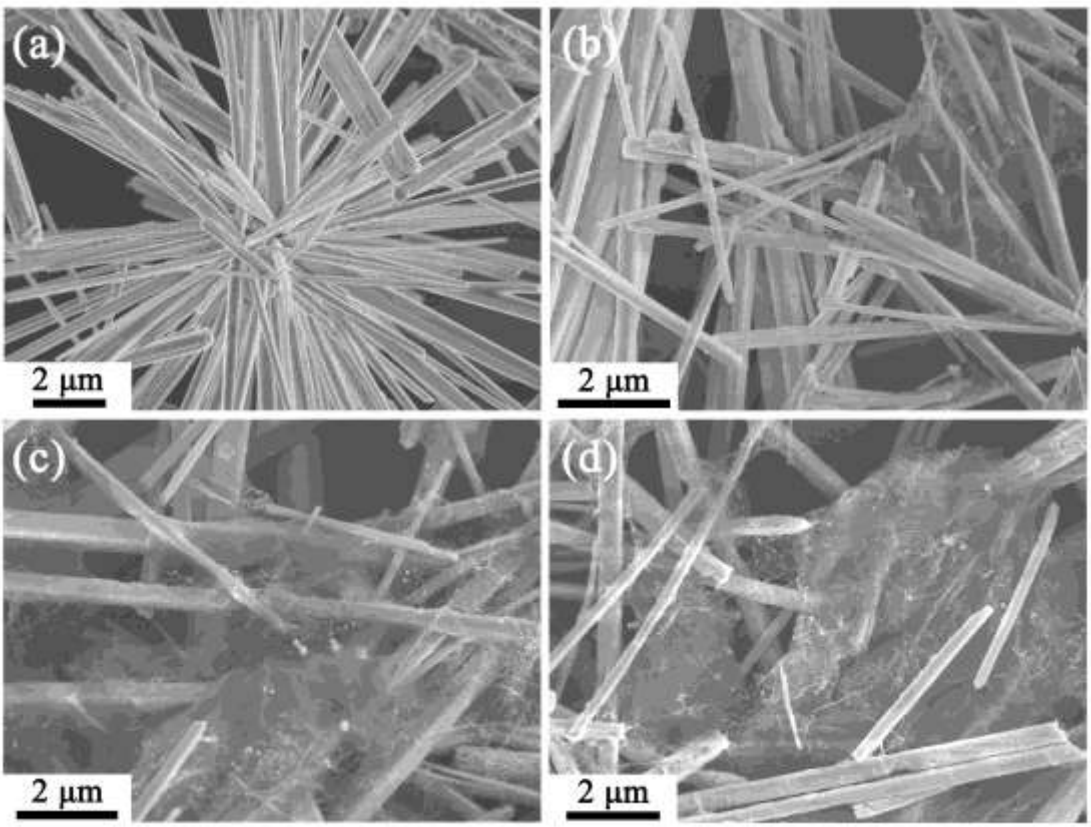

Fig. 1. SEM images of the as-prepared (a) α-$AgVO_3$, (b) 0.5 GO/α-$AgVO_3$, (c) 1.0 GO/α-$AgVO_3$, (d) 2.0 GO/α-$AgVO_3$.

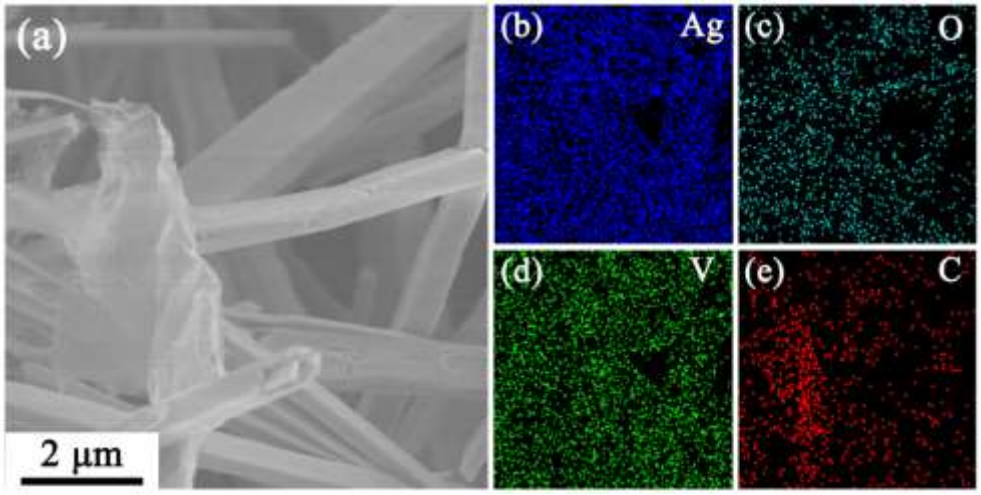

Fig. 2. The SEM image of 0.5 GO/α-$AgVO_3$ (a) and the corresponding EDS elemental mapping of (b) Ag, (c) O, (d)V, and (e) C.

3.2. Crystal structure and XRD analysis

The phase composition and preferred grow direction of α-$AgVO_3$ nanorods were further studied by experimental and simulated XRD patterns. The XRD patterns of the as-prepared α-$AgVO_3$ and GO/α-$AgVO_3$ are shown in **Fig. 3**. The α-$AgVO_3$ is well crystallized in a monoclinic structure and no impurity phase can be detected. The main peaks at 2θ degrees of 12.40 °, 17.22 °, 24.95 °, 27.50 °, 28.23 °, 31.51 °, 32.12 °, and 32.82 ° can be ascribed to (110), (200), (220), (310), ($\bar{2}$21), (221), ($\bar{1}$31) and (002) diffraction planes of α-$AgVO_3$ (according to JCPDS card #89-4396), respectively. After the introduction of GO, the 2θ angles of each diffraction peak remains unchanged, indicating that the addition of GO does not affect the phase stability and crystal structure of α-$AgVO_3$. Due to the low percentage and weak reflection of GO, no obvious diffraction peak for GO can be observed in the XRD pattern of GO/α-$AgVO_3$.

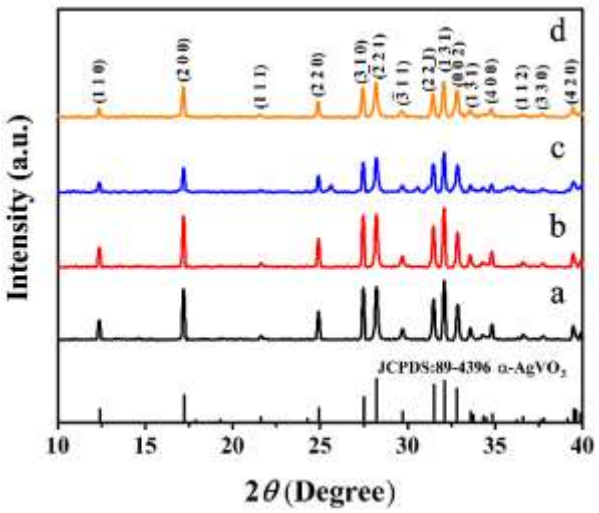

Fig. 3. XRD patterns of (a) α-$AgVO_3$, (b) 0.5 GO/α-$AgVO_3$, (c) 1.0 GO/α-$AgVO_3$ and (d) 2.0 GO/α-$AgVO_3$.

To reveal the growth orientation of α-$AgVO_3$ nanorods, its crystal structure was constructed and optimized (**Fig.4** and **Table.1**), and the comparison of the simulated and experimental XRD patterns of α-$AgVO_3$ is shown in **Fig. 5**. **Fig.4** shows that two VO_4 tetrahedrons are connected by sharing vertex and then precipitate with Ag to crystallize in a monoclinic α phase $AgVO_3$ with space group *C 2/c*. The geometry optimized lattice constants, atomic positions and bond lengths of α-$AgVO_3$ are shown in **Table.1**.

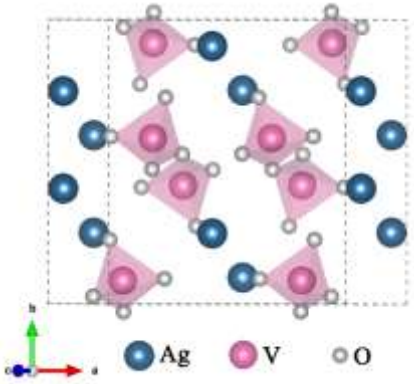

Fig. 4. Crystal structure of α-$AgVO_3$.

Table 1. Geometry optimized lattice constants, atomic positions and bond lengths of α-$AgVO_3$.

Parameter	α-$AgVO_3$		
Space group	*C 2/c* (No.15)		
Lattice constants	a = 11.2975 Å b = 10.7962 Å c = 5.78487 Å V = 646.534 Å^3		
Atomic positions	V1 (0.30349, 0.41734, 0.26496) Ag1 (0, 0.25195, 0.25) Ag2 (0, 0.59393, 0.25) O1 (0.13789, 0.41143, 0.14139) O2 (0.14649, 0.027, −0.02306) O3 (0.36723, 0.27405, 0.36506)		
Bond lengths	Bond	Population	Length (Å)
	O-V	0.73	1.70684
	O-V	0.73	1.71587
	O-Ag	0.22	2.17526
	O-Ag	0.24	2.14763
	O-O	0.00	2.81117

Based on this geometry optimized crystal structure, the XRD pattern simulation was carried out through the Reflex code in Materials Studio software (Accelrys Software Inc., San Diego, CA, USA) using Cu*Kα* radiation of $\lambda = 1.5406$Å, step size of 0.02° . The preferred *c*-axis orientation was imposed by the Rietveld-Toraya method and the simulated morphology was calculated based on the theory of Donnay-Harker [25-27]. According to Scherrer's formula, the grain size difference in different directions will result in different broadening degree of diffraction peaks. Thus, as shown in **Fig. 5**, the simulated XRD pattern of α-$AgVO_3$ nanorods with a growth direction that perpendicular to the (002) crystal plane is closer to the experimental result, compared with that of the power reflection without orientation. Meanwhile, the simulated morphology shown in **Fig.5(d)** further confirms that the α-$AgVO_3$ nanorods prefers to growth along *c*-axis that perpendicular to (002) crystal

plane.

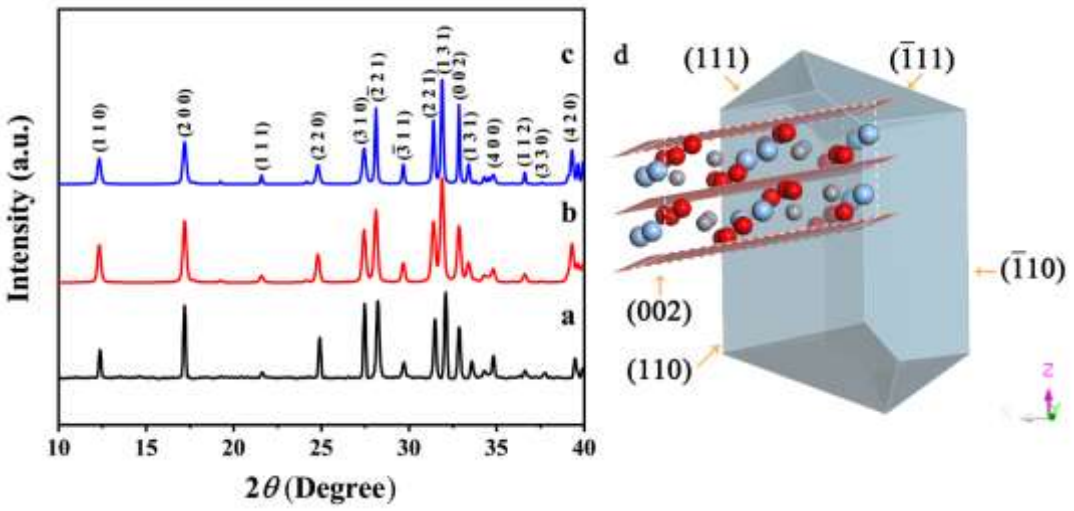

Fig. 5. Experimental XRD patterns of α-$AgVO_3$ (a), together with simulated XRD patterns of powder (b) and *c*-axis oriented particle (c). (d) the calculated morphology based on the theory of Donnay-Harker. (The purple crystal is the α-$AgVO_3$ nanorod, and the plane is the (0 0 2) plane.)

3.3. FTIR and Raman characterization

In order confirm the presence of GO in the GO/α-$AgVO_3$ photocatalysts, Fourier transform infrared spectroscopy (FTIR Spectroscopy) and Raman spectroscopy were employed. As shown in the FTIR spectra **(Fig. 6a)**, the bands related to the VO_4 tetrahedron, including ν (V−O−V) (515 cm^{-1}), δ (V−O) (636 cm^{-1}), and ν (V=O) (660, 895, 929, and 964 cm^{-1}) vibrational modes are observed, as well as bands at 846 cm^{-1} for ν (Ag−O−V) stretching modes [28,29]. For GO/α-$AgVO_3$, in addition to the bands mentioned above, typical peaks of C−O stretching and C−C sp^2 in-plane vibration emerge at 1057 cm^{-1} and 1624 cm^{-1}, demonstrating the successfully introduction of GO [30]. In fact, GO is more sensitive to Raman spectroscopy. As shown in **Fig. 6b**, two typical GO peaks at about 1340 and 1597 cm^{-1} appear in the spectra of

GO/α-$AgVO_3$, which are attributed to the disordered sp^2 carbon (D-band) and well-ordered graphite (G-band) respectively [31, 32]. With the increase of GO contents, the intensity of D and G peaks also increase. Moreover, the main characteristic vibration peaks of α-$AgVO_3$ are all observed as well. In Raman spectra of all the samples, the strongest band at 919 cm^{-1} may originate from symmetric stretching of V–O–Ag or O–V–O vibrations. The band at 897 cm^{-1} is linked with the stretching vibrations of Ag–O–Ag, while the band at 875 cm^{-1} represents the stretching vibrations of the V–O–Ag. The bands appearing at 850, 762, 627, and 528 cm^{-1} are related to the asymmetric and symmetric stretching modes of V–O–V [33-35]. Based on the FTIR and Raman spectra results, the composition of GO/α-$AgVO_3$ are further confirmed. All the foregoing results demonstrate that a serial of α-$AgVO_3$ (002) // GO (002) heterostructure photocatalysts have been successfully prepared.

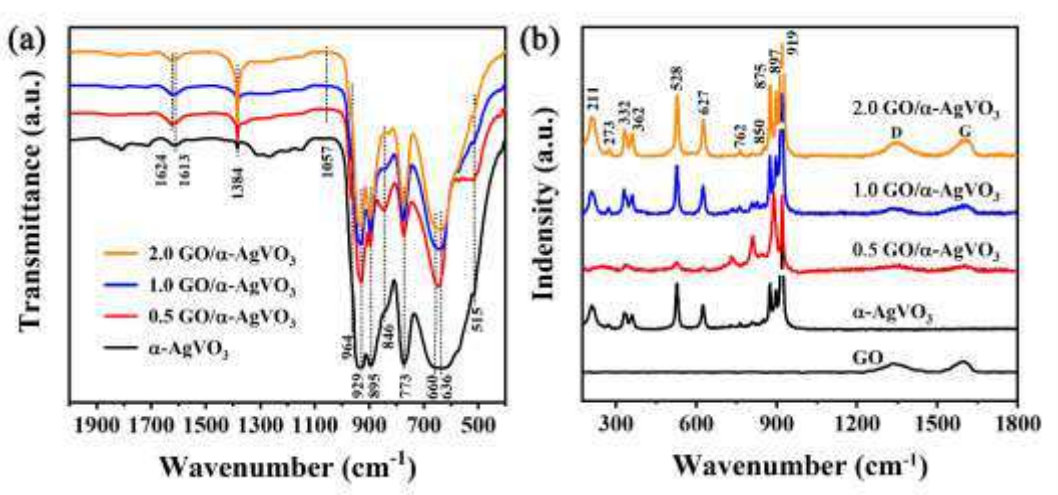

Fig. 6. (a) FTIR spectra and (b) Raman spectra of α-$AgVO_3$ and GO/α-$AgVO_3$ with different GO contents (in 0.5 wt.%, 1.0 wt.%, and 2.0 wt.%).

3.4. Photocatalytic performance

The photocatalytic activities of α-$AgVO_3$ and GO/α-$AgVO_3$ are evaluated in terms of the photodegradation of RhB. **Fig. 7(a)** shows the variation of RhB concentration with irradiation time of visible light. It is obvious that the introduction of GO significantly improves the photocatalytic performance compared with pure α-$AgVO_3$. After 40 min of irradiation, the 0.5 GO/α-$AgVO_3$ photocatalyst displays the highest photocatalytic activity with 90.0% RhB degradation, while few RhB is removed by pure α-$AgVO_3$. Quantitatively, the photocatalytic degradation of RhB can be described by pseudo-first-order dynamic process and its kinetics can be expressed as:

$$ln\left(\frac{C_0}{C}\right) = k_1 t \quad (1)$$

where C is the concentration of the RhB at time t, C_0 is the initial concentration of the RhB solution, and the slope k_1 is the apparent reaction rate constant. As shown in **Fig. 7(b)**, the 0.5 GO/α-$AgVO_3$ photocatalyst has the maximum rate constant of 0.0584 min^{-1} which is 18 times higher than that of pure α-$AgVO_3$, revealing the superior photocatalytic activity of the GO/α-$AgVO_3$. With the increase of GO contents, the degradation efficiency decreases probably due to the aggregation of GO nanosheets as shown in SEM images in **Fig. 1**. Compared with the performance of other SVOs and traditional TiO_2 photocatalysts under the similar experimental conditions [16,36-42], the GO/α-$AgVO_3$ photocatalyst shows outstanding performance with fast rate and large degradation ratio as shown in **Table 2**.

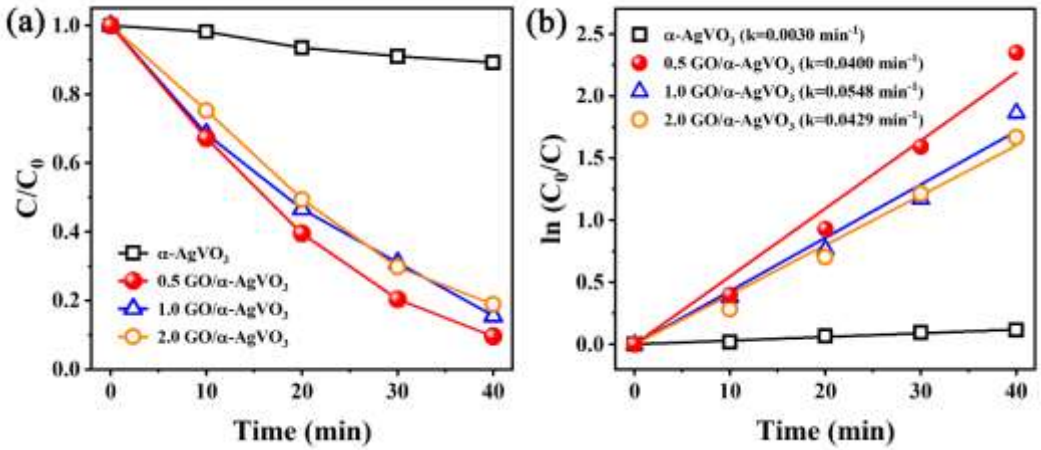

Fig. 7. Photocatalytic degradation curves of RhB (a) and the corresponding pseudo-first-order kinetic curves (b).

Table 2. RhB photodegradation properties of recently reported SVOs and other photocatalysts.

Photocatalyst	Loading (Photocatalyst/Dye)	Degradation ratio [a]	Apparent rate constant k (min^{-1})	Reference
TiO_2	100 mg / 1 mg	12%	0.0060	Wang, *et al* [36]
α-$AgVO_3$/α-FeOOH	50 mg / 0.24 mg	45%	0.0194	Sun, *et al* [16]
β-$AgVO_3$/Ag_3VO_4	50 mg / 0.3 mg	76%	0.0340	Gao, *et al* [37]
β-$AgVO_3$/$BiVO_4$	50 mg / 1 mg	69%	0.0206	Wang, *et al* [38]
β-$AgVO_3$/AgBr	30 mg / 0.5 mg	23%	0.0183	Zhang, *et al* [39]
$Ag_4V_2O_7$	80 mg / 0.38 mg	38%	–	Wang, *et al* [40]
g-C_3N_4/ $Ag_4V_2O_7$	100 mg/ 1mg	55%	0.015	Zhang, *et al* [41]
Ag_3VO_4	2 g / 4.8 mg	32%	0.0155	Zhang, *et al* [42]
GO/α-$AgVO_3$	15 mg / 0.15 mg	90%	0.0584	This work

[a] The degradation percentage is collected at 40 min visible-light irradiation for better comparison.

4. Discussion

4.1. Electronic structure and bandgaps

To shed light on the photocatalytic mechanism, it is necessary to analyze the electronic structure of α-$AgVO_3$. **Fig. 8** shows the band structure of α-$AgVO_3$ along the high symmetry line in the Brillouin zone calculated by GGA (**Fig.8a**) and HSE03 functional (**Fig.8b**), respectively. The α-$AgVO_3$ is a direct band gap semiconductor

because the top of valence bands and bottom of conduction bands are at the Gamma point simultaneously. The direct band gap of α-$AgVO_3$ obtained from GGA functional is 1.9 eV because the GGA functional generally underestimated the experimental band gaps. To improve the accuracy of band gap calculation, a hybrid functional [43] based on a screened Coulomb potential HSE03 was used in DFT calculation. As shown in **Fig. 8(b)**, the band gap obtained by HSE03 functional is 3.0 eV which is believed more reliable and closer to the experimental values for complex oxides [24,44].

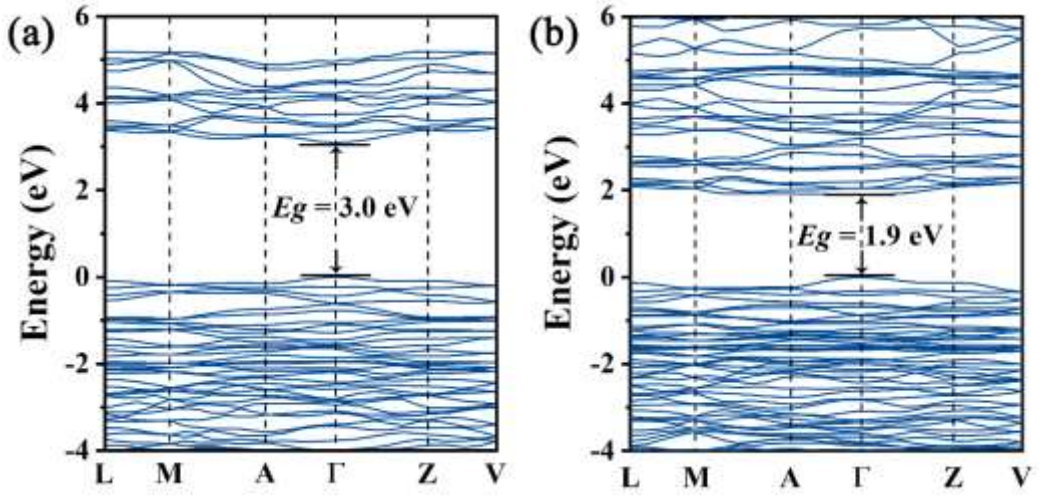

Fig. 8. Band structure of α-$AgVO_3$ along the high symmetry line in the Brillouin zone calculated by (a) GGA and (b) HSE03 functional.

To analyze the optical properties and obtain the experimental bandgaps, UV–vis absorption spectra of α-$AgVO_3$ and GO/α-$AgVO_3$ nanorods are collected. As shown in **Fig. 9(a)**, the absorbance edge of α-$AgVO_3$ is around 540 nm. After the introduction of 0.5 and 1.0 wt.% GO, the absorption band edge shows an obvious red-shift to the visible-light region, indicating that a small amount of GO is helpful for visible light absorption. However, 2.0 wt.% GO addition causes the absorption band edge to shift in the opposite direction, i.e., visible-light absorption and performance

are weakened, which is consistent with the photocatalysis activities.

The band gap of α-$AgVO_3$ can be obtained by the Kubelka–Munk method [45].

$$(\alpha hv)^n = A(hv - E_g) \quad (2)$$

where α, h, v, A, and E_g are the absorption coefficient, Planck's constant, light frequency, proportionality constant, and optical bandgap, respectively. The index n depends on the electronic transition of the crystalline semiconductor, n = 0.5 for indirect-gap semiconductor and n = 2 for direct-gap semiconductor. For α-$AgVO_3$ crystal, n equals 2, because α-$AgVO_3$ is a direct transition type of semiconductors, according to the band structure in **Fig. 8**. The Kubelka−Munk plots are shown in **Fig. 9(b)**. The band gap energy can be estimated from the intercept of the tangent to the plot of $(\alpha hv)^2$ vs energy (hv). The band gap of α-$AgVO_3$ is 2.56 eV, which is approximate to the calculated bandgap from HSE03. The bandgaps for 0.5, 1.0 and 2.0 GO/α-$AgVO_3$ are 2.59, 2.62, and 2.26 eV, i.e., the addition of 0.5 and 1.0 wt.% GO can help to increase the band gap, which is beneficial for the separation of photogenerated carriers. However, continues to increase the GO content will narrow the band gap due to the conductive nature of GO, resulting in the decrease of photocatalytic performance. Therefore, the theoretical and experimental analysis of band structure demonstrates that α-$AgVO_3$ is a visible-light-responsible photocatalyst, and the combination with an appropriate amount of GO helps to expand the absorption of visible light and improve the photocatalytic efficiency.

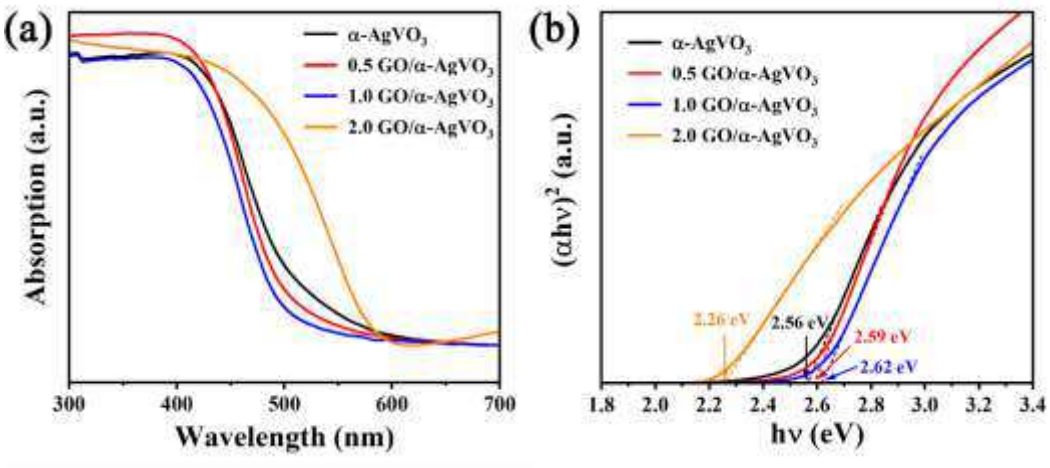

Fig. 9. UV−vis diffuse reflectance spectra (a) and Kubelka−Munk plot (b) of α-$AgVO_3$ and GO/α-$AgVO_3$ with different GO contents (in 0.5 wt.%, 1.0 wt.%, and 2.0 wt.%).

To further analyze the band structure, ultraviolet photoelectron spectroscopy (UPS) is implemented to ascertain the valence band energy (E_v), as shown in **Fig. 10(a)**. The E_v of α-$AgVO_3$ is calculated to be 6.61 eV via subtracting the width of the UPS spectra from the excitation energy of 21.22 eV [46]. The conduction band energy (E_c) is thus estimated at 4.05 eV from the equation: $E_C = E_V - E_g$. Considering the reference standard for which 0 eV vs. NHE (Normal hydrogen electrode) equals -4.44 eV vs. E_{avs} (Vacuum level), the E_V and E_C of α-$AgVO_3$ are converted to -0.39 and 2.27 eV (vs. NHE) [47]. The energy position of α-$AgVO_3$ is illustrated in **Fig. 10(b)** [48], which provides clear guidance for the subsequent proposal of the photocatalytic mechanism.

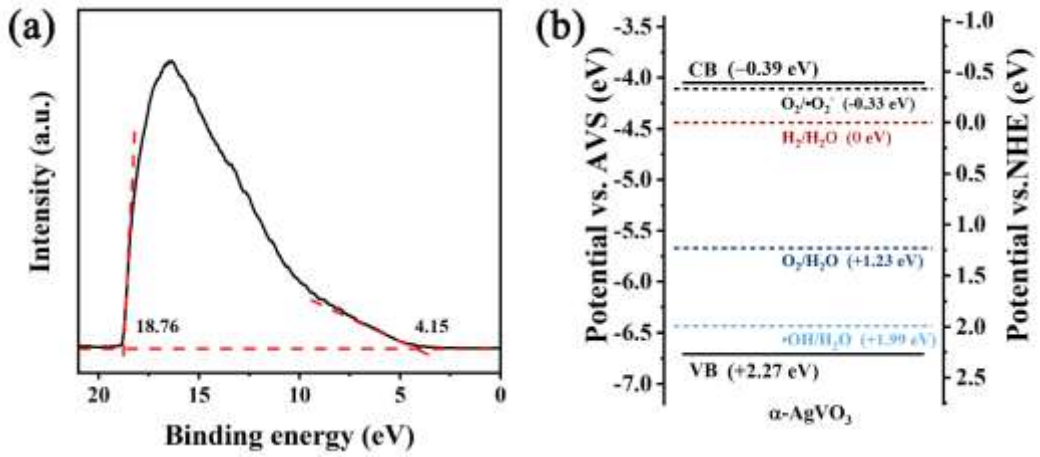

Fig. 10. UPS spectra (a) and the band structure diagram of α-$AgVO_3$(b).

4.2. The role of GO/α-$AgVO_3$ heterojunction

According to the structure and morphology characterization and simulated morphology in section 3, the α-$AgVO_3$ (002) // GO (002) heterojunction is successfully constructed in the GO/α-$AgVO_3$ photocatalyst. The surface chemical composition and the interaction of GO and α-$AgVO_3$ were further confirmed by XPS. The full range XPS spectrum in **Fig. 11(a)** confirms the presence of C, Ag, V, and O elements in the 0.5 GO/α-$AgVO_3$ without impurities. The high-resolution XPS spectra of Ag 3*d*, V 2*p*, and O 1*s* are shown in **Fig. 11(b-d)**. In **Fig. 11(b)**, the peaks that emerged at the binding energy of 367.5 eV and 373.5eV correspond to Ag $3d_{5/2}$ and Ag $3d_{3/2}$ orbits. The XPS spectra of V 2*p* show two specific peaks of pentavalent vanadium at the binding energy of 516.4 eV and 523.8 eV [49], as shown in **Fig.11(c)**. The O 1*s* spectra shown in **Fig.11(d)** can be split into three peaks at 529.9 eV, 530.4 eV, and 532.1 eV, which are attributed to the binding energies of lattice oxygen, oxygen defects and adsorbed oxygen species [50]. After the introduction of GO, a new C=O peak appears at 533.4 eV in the O 1*s* spectrum [51]. More importantly,

peaks of Ag 3*d*, V 2*p*, and O1*s* in 0.5, 1.0, and 2.0 GO/α-$AgVO_3$ are all shifted towards the high binding energy, indicating the electron migration from α-$AgVO_3$ to GO nanosheet happens, which can improve the separation efficiency of photogenerated carriers and enhance photocatalytic performance [12].

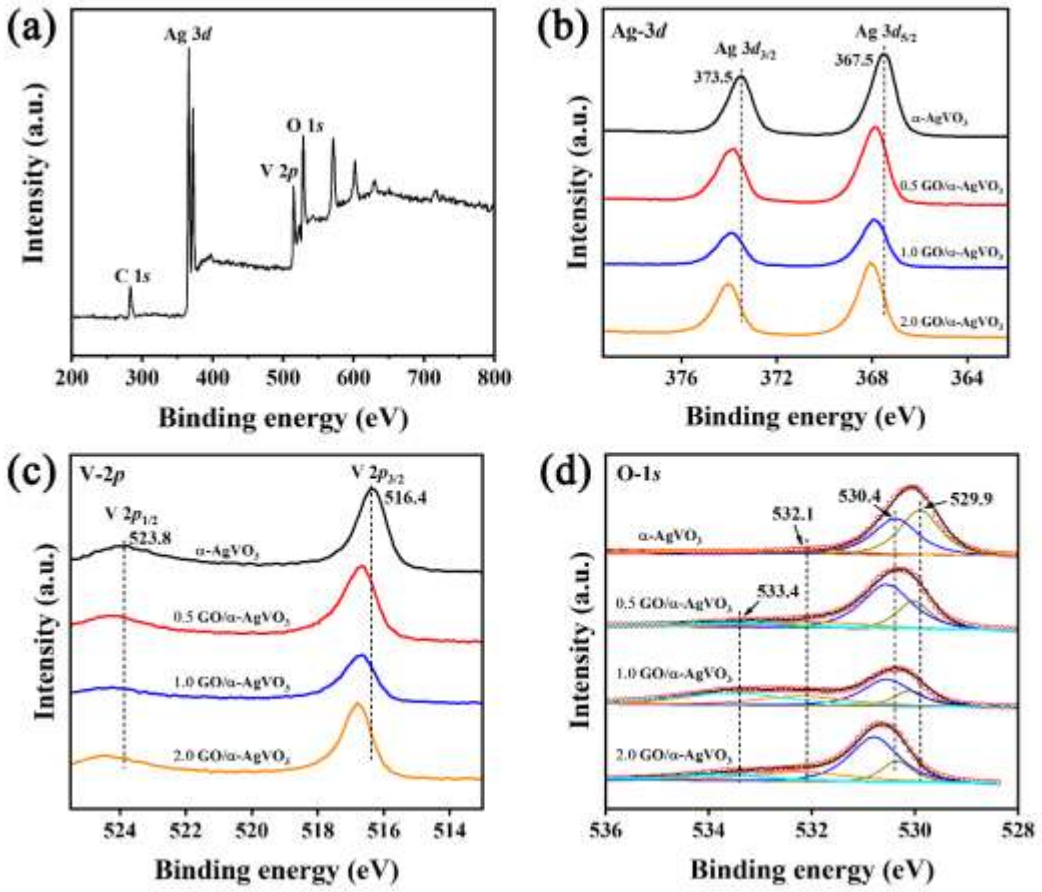

Fig 11. Full-scale XPS survey spectrum for 0.5 GO/α-$AgVO_3$ (a) and the XPS spectra of (b) Ag 3*d*, (c) V 2*p* and O 1*s* for GO/α-$AgVO_3$ with different GO contents (in 0.5 wt.%, 1.0 wt.%, and 2.0 wt.%).

4.3. Mechanism for the enhanced photocatalytic performance of the GO/α-$AgVO_3$

Based on the foregoing analysis, the possible mechanism of the GO/α-$AgVO_3$ photocatalyst is proposed and illustrated in **Fig. 12**. When the visible-light shines on the surface of GO/α-$AgVO_3$ photocatalyst, the electrons (e^-) at valance band (VB) are

excited to conduct band (CB), leaving an equal number of holes (h^+) at VB, as presented in equation (3). The electrons in the conduction band of α-$AgVO_3$ can transfer to the surface of GO through the α-$AgVO_3$ (002) // GO (002) heterojunction, promoting the separation efficiency of photogenerated carriers. Taking advantage of the conductivity of GO's π–π graphitic carbon network, the lifetime of electrons can be further prolonged [52], which is helpful to improve the photocatalytic performance. Then, the h^+ at VB can produce hydroxyl radicals (•OH) by reacting with H_2O, while the e^- at GO can generate superoxide radicals. These radicals and holes with high oxidative activity can degrade organic pollutants like RhB efficiently by the possible equations as follow:

$$\alpha\text{-}AgVO_3 + h\nu \rightarrow \alpha\text{-}AgVO_3\ (e^- + h^+) \quad (3)$$

$$e^-\ (\alpha\text{-}AgVO_3) + GO \rightarrow \alpha\text{-}AgVO_3 + \text{injected } e^-\ (GO) \quad (4)$$

$$\alpha\text{-}AgVO_3\ (h^+) + H_2O \rightarrow \bullet OH + H^+ \quad (5)$$

$$e^-\ (GO/\alpha\text{-}AgVO_3) + O_2 \rightarrow \bullet O^{2-} \quad (6)$$

$$RhB + \alpha\text{-}AgVO_3\ (h^+)/\bullet O^{2-}/\bullet OH \rightarrow \text{intermediates} \rightarrow CO_2 + H_2O \quad (7)$$

Therefore, suitable band structure and band gap for visible light absorption are fundamental factors for visible-light-responsive photocatalyst, and their photocatalytic performances can be further improved by inhibiting the recombination of photogenerated carriers through heterostructure design.

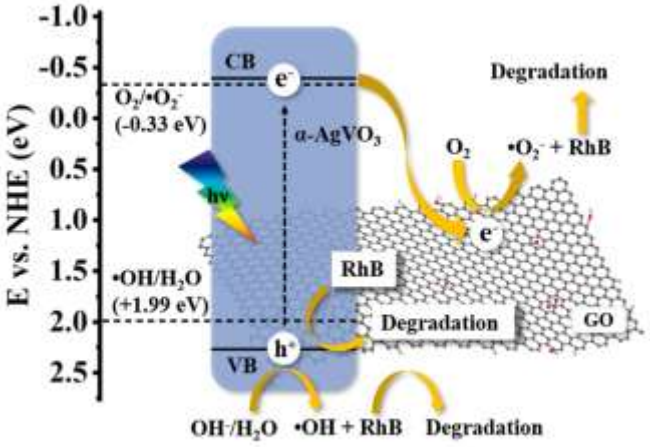

Fig. 12. Proposed photocatalytic mechanism of GO/α-$AgVO_3$ photocatalyst.

5. Conclusions

In summary, novel visible-light-responded photocatalysts including 0.5wt% GO/α-$AgVO_3$, 1.0wt% GO/α-$AgVO_3$, 2.0wt% GO/α-$AgVO_3$, and pure α-$AgVO_3$ were successfully synthesized by a facile in-situ coprecipitation method, and their structure, morphology, photocatalytic performance and mechanism were revealed. SEM analyses indicate that the as-prepared photocatalysts have a flower-like morphology, wherein the petals consist of α-$AgVO_3$ nanorods with a length of a few microns and then GO nanosheets are uniformly covered on these nanorods. XRD analyses demonstrate that α-$AgVO_3$ is well crystallized in a monoclinic α phase with space group *C 2/c*. Through the reflex stimulation, it can be confirmed that the α-$AgVO_3$ nanorods prefer to grow along the *c* axis. Raman, FTIR, and XPS spectra demonstrate the existence of GO nanosheets, and finally, confirm the formation of α-$AgVO_3$ (002) // GO (002) heterojunction. The successful introduction of GO nanosheets and construction of heterostructure might have unique effect on the photocatalytic performance.

Compared with pure α-$AgVO_3$ and other SVOs, 0.5 GO/α-$AgVO_3$ displays the optimal photodegradation efficiency of 90% RhB removal with the maximum rate constant of 0.0584 min^{-1} which is tens of times higher than that of pure α-$AgVO_3$ and other SVOs. Proper band gap and efficient photocarrier separation play significant roles in high photocatalytic performance of GO/α-$AgVO_3$. Electronic structure and band gap calculation by HSE03 functional and optical properties analysis reveals that is α-$AgVO_3$ a direct-gap semiconductor with a band gap of about 2.56 eV which is suitable for visible light absorption and irradiation. Then, the GO and α-$AgVO_3$ heterojunction facilitates the transfer of photogenerated electrons, which overcomes the obstacle of rapid recombination of carriers and further boosts the photocatalytic activity. Moreover, some active species like h^+, $\bullet O^{2-}$ and •OH generated by the photochemical reaction can help degrade organic pollutants like RhB. With the advantage of suitable band gap, efficient photocarriers separation and superior photocatalytic performance, GO/α-$AgVO_3$ is a promising photocatalyst for the visible-light degradation of pollutants and water environmental protection.

Acknowledgement

The authors gratefully acknowledge the financial support of the key laboratory Foundation of the Science and Technology on Advanced Functional Composite Laboratory (Grant No. 6142906200509), the Natural Science foundation of Jiangsu Province Colleges (Grant No. 20KJB430017) and NUPTSF (Grant No. NY219162).

References

1.Low J, Yu J, Jaroniec M, *et al*. Heterojunction photocatalysts. *Adv Mater* 2017, **29**: 1601694.

2.Ju P, Wang Y, Sun Y, *et al*. In-situ green topotactic synthesis of a novel Z-scheme Ag@$AgVO_3$/$BiVO_4$ heterojunction with highly enhanced visible-light photocatalytic activity. *J Colloid Interf Sci* 2020, **579**: 431-447.

3.Jeong S Y, Shin HM, Jo YR, *et al*. Plasmonic silver nanoparticle-impregnated nanocomposite $BiVO_4$ photoanode for plasmon-enhanced photocatalytic water splitting. *J Phys Chem C* 2018, **122**: 7088-7093.

4.Sadeghzadeh-Attar A. Photocatalytic degradation evaluation of N-Fe codoped aligned TiO_2 nanorods based on the effect of annealing temperature. *J Adv Ceram* 2020, **9**: 107-122.

5.Su T, Shao Q, Qin Z, *et al*. Role of interfaces in two-dimensional photocatalyst for water splitting. *ACS Catal* 2018, **8**: 2253-2276.

6.Nomikos GN, Panagiotopoulou P, Kondarides DI, *et al*. Kinetic and mechanistic study of the photocatalytic reforming of methanol over Pt/TiO_2 catalyst. *Appl Catal B Environ* 2014, **146**: 249-257.

7.Zhao W, Guo Y, Wang S, *et al*. A novel ternary plasmonic photocatalyst: ultrathin g-C_3N_4 nanosheet hybrided by Ag/$AgVO_3$ nanoribbons with enhanced visible-light photocatalytic performance. *Appl Catal B Environ* 2015, **165**: 335-343.

8.Shi R, Ye HF, Liang F, *et al*. Interstitial P-doped CdS with long-lived photogenerated electrons for photocatalytic water splitting without sacrificial agents. *Adv Mater* 2018, **30**: 1705941.

9.Zhang S, Li J, Wang X, *et al*. Rationally designed 1D Ag@$AgVO_3$ nanowire/graphene /protonated g-C_3N_4 nanosheet heterojunctions for enhanced photocatalysis via electrostatic self-assembly and photochemical reduction methods. *J Mater Chem A* 2015, **3**: 10119-10126.

10.Chen Y, Liang Y, Zhao M, *et al*. In situ ion exchange synthesis of Ag_2S/$AgVO_3$ graphene aerogels for enhancing photocatalytic antifouling efficiency. *Ind Eng Chem Res* 2019, **58**: 3538-3548.

11.Huang CM, Pan GT, Li YCM, *et al*. Crystalline phases and photocatalytic activities of hydrothermal synthesis Ag_3VO_4 and $Ag_4V_2O_7$ under visible light irradiation. *Appl Catal A Gen* 2009, **358**: 164-172.

12.Ran R, Meng X, Zhang Z. Facile preparation of novel graphene oxide-modified Ag_2O/Ag_3VO_4/$AgVO_3$ composites with high photocatalytic activities under visible light irradiation. *Appl Catal B Environ* 2016, **196**: 1-15.

13.Shen G, Chen D. Self-Coiling of $Ag_2V_4O_{11}$ Nanobelts into Perfect Nanorings and Microloops. *J Am Chem Soc* 2006, **128**: 11762-11763.

14. Zhao W, Guo Y, Faiz Y, *et al*. Facile in-suit synthesis of Ag/$AgVO_3$ one-dimensional hybrid nanoribbons with enhanced performance of plasmonic visible-light photocatalysis. *Appl Catal B Environ* 2015, **163**: 288-297.

15. Yang Y, Liu Y, Huang B, *et al*. Enhanced visible photocatalytic activity of a $BiVO_4$@β-$AgVO_3$

composite synthesized by an in situ growth method. *RSC Adv* 2014, **4**: 20058-20061.

16.Sun M, Senthil RA, Pan J, *et al*. A Facile synthesis of visible-light driven Rod-on-Rod like α-FeOOH/α-$AgVO_3$ nanocomposite as greatly enhanced photocatalyst for degradation of Rhodamine B. *Catalysts* 2018, **8**:392.

17.Chen LC, Teng CY, Lin CY, *et al*. Architecting nitrogen functionalities on graphene oxide photocatalysts for boosting hydrogen production in water decomposition process. *Adv Energy Mater* 2016, **6**: 1600719.

18.Huang Y and Wan C. Controllable fabrication and multifunctional applications of graphene/ceramic composites. *J Adv Ceram* 2020, **9**: 271-291.

19.Tian H, Liu M, Zheng W. Constructing 2D graphitic carbon nitride nanosheets/layered MoS_2/graphene ternary nanojunction with enhanced photocatalytic activity. *Appl Catal B Environ* 2018, **225**: 468-476.

20.Clark SJ, Segall MD, Pickard CJ, *et al*. First principles methods using CASTEP. *Z. Kristallog*r 2005, **220**: 567-570.

21.Segall MD, Lindan P, Probert MJ, *et al*. First-principles simulation: ideas, illustrations and the CASTEP code. *J Phys: Condens Mater* 2002, **14**:2717-2744.

22.Pack JD, Monkhorst HJ. Special points for Brillouin-Zone inte-grations-A Reply. *Phys Rev B* 1977, **16**:1748-1749.

23.Perdew JP, Burke K, Ernzerhof M, Generalized gradient approximation made simple. *Phys Rev Lett* 1996. **77**: 3865-3868.

24.Zhou Y and Xiang H. Al_5BO_9: A wide band gap, damage-tolerant, and thermal insulating lightweight material for high-temperature applications. *J Am Chem Soc* 2016, **99**:2742-2751.

[25] J. Donnay and D. Harker, A new law of crystal morphology extending the Law of Bravais, *Am Mineral* 1937, **22**: 457-477.

[26] A. F. Wells, XXI. Crystal habit and internal structure.-I, *The London, Edinburgh, and Dublin Philosophical Magazine and Journal of Science* 1946, **37**:184-199.

[27] Z. Berkovitch-Yellin, Toward an ab initio derivation of crystal morphology, *J.Am.Chem.Soc* 1985, **107**: 8239-8253.

28.Sivakumar V, Suresh R, Giribabu K, *et al*. $AgVO_3$ nanorods: Synthesis, characterization and visible light photocatalytic activity. *Solid State Sci* 2015, **39**: 34-39.

29.Barebita H, Ferraa S, Moutataouia M, *et al*. Structural investigation of Bi_2O_3-P_2O_5-B_2O_3-V_2O_5 quaternary glass system by Raman, FTIR and thermal analysis. *Chem Phys Lett* 2020, **760**: 138031.

30.Li Q, Guo B, Yu J, *et al*. Highly Efficient Visible-light-driven photocatalytic hydrogen production of CdS-cluster-decorated graphene nanosheets. *J Am Chem Soc* 2011, **133**: 10878-10884.

31.Wang H, Robinson JT, Li X, *et al*. Solvothermal reduction of chemically exfoliated graphene sheets. *J Am Chem Soc* 2009, **131**: 9910-9911.

32.Zhao W, Li J, Wei Z b, *et al*. Fabrication of a ternary plasmonic photocatalyst of Ag/$AgVO_3$/RGO and its excellent visible-light photocatalytic activity. *Appl Catal B Environ* 2015, **179**: 9-20.

33.Kong X, Guo Z, Zeng C, *et al*. Soft chemical in situ synthesis, formation mechanism and electrochemical performances of 1D bead-like $AgVO_3$ nanoarchitectures. *J Mater Chem A* 2015, **3**: 18127-18135.

34.Oliveira RC, Foggi CC, Teixeira MM, *et al*. Mechanism of antibacterial activity via morphology change of α-$AgVO_3$: Theoretical and experimental insights. *ACS Appl Mater Interfaces* 2017, **9**: 11472-11481.

35.Song JM, Lin YZ, Yao HB, *et al*. Superlong β-$AgVO_3$ nanoribbons: High-yield synthesis by a pyridine-assisted solution approach, their Stability, electrical and electrochemical properties. *ACS Nano* 2009, **3**: 653-660.

36.Wang F, Li F, Zhang L, *et al*. S-TiO_2 with enhanced visible-light photocatalytic activity derived from TiS_2 in deionized water. *Mater Res Bull* 2017, **87**: 20-26.

37.Gao L, Li Z, Liu J. Facile synthesis of Ag_3VO_4/β-$AgVO_3$ nanowires with efficient visible-light photocatalytic activity. *RSC Adv* 2017, **7**: 27515-27521.

38.Wang R and Cao L. Facile synthesis of a novel visible-light-driven $AgVO_3$/$BiVO_4$ heterojunction photocatalyst and mechanism insight. *J Alloys Compd* 2017, **722**: 445-451.

39.Zhang J, Wang J, Xu H, *et al*. The effective photocatalysis and antibacterial properties of AgBr/$AgVO_3$ composites under visible-light. *RSC Adv* 2019, **9**: 37109-37118.

40. Wang J, Yang X, Chen J, *et al*. Photocatalytic activity of novel $Ag_4V_2O_7$ photocatalyst under visible light irradiation. *J Am Ceram Soc* 2014, **97**: 267-274.

41. Zhang T, Zhao D, Wang Y, *et al*. Facial synthesis of a novel $Ag_4V_2O_7$/g-C_3N_4 heterostructure with highly efficient photoactivity. *J Am Ceram Soc* 2019,**102**:3897-3907.

42. Zhang L, He Y, Ye P, *et al*. Enhanced photodegradation activity of Rhodamine B by Co_3O_4/Ag_3VO_4 under visible light irriadiation. *Mat Sci Eng B* 2013, **178**: 45-52.

43.Perdew JP, Ruzsinszky A, Csonka GI, *et al*. Restoring the density-gradient expansion for exchange in solids and surfaces. *Phys Rev Lett* 2008, **100**: 136406.

44.Heyd J, Scuseria GE, Ernzerhof M. Hybrid functionals based on a screened Coulomb potential. *J Chem Phys* 2003, **118**: 8207-8215.

45.Tandon SP and Gupta JP. Measurement of forbidden energy gap of semiconductors by diffuse reflectance technique. *Phys Status Solidi B* 1970, **38**: 363-367.

46.Liu J, Liu Y, Liu N, *et al*. Metal-free efficient photocatalyst for stable visible water splitting via a two-electron pathway. *Science* 2015, **347**: 970.

47.Wu X, Zhao J, Wang L, *et al*. Carbon dots as solid-state electron mediator for $BiVO_4$/CDs/CdS Z-scheme photocatalyst working under visible light. *Appl Catal B Environ* 2017, **206**: 501-509.

48.Zheng Y, Yu Z, Ou H, *et al*. Black phosphorus and polymeric carbon nitride heterojunction for photoinduced molecular oxygen activation. *Adv Funct Mater* 2018, **28**: 1705407.

49.Luo G, Jiang X, Li M, *et al*. Facile fabrication and enhanced photocatalytic performance of Ag/AgCl/rGO heterojunction photocatalyst. *ACS Appl Mater Inter* 2013, **5**: 2161-2168.

50.Liu D, Chen D, Li N, *et al*. Integration of 3D macroscopic graphene aerogel with 0D-2D $AgVO_3$-g-C_3N_4 heterojunction for highly efficient photocatalytic oxidation of nitric oxide. *Appl Catal B Environ* 2019, **243**: 576-584.

51.Ran R, McEvoy JG, Zhang Z. $Ag_2O/Ag_3VO_4/Ag_4V_2O_7$ heterogeneous photocatalyst prepared by a facile hydrothermal synthesis with enhanced photocatalytic performance under visible light irradiation. *Mater Res Bull* 2016, **74**: 140-150.

52.Cao S, Liu T, Tsang Y, *et al*. Role of hydroxylation modification on the structure and property of reduced graphene oxide/TiO_2 hybrids. *Appl Surf Sci* 2016, **382**: 225-238.

Figures

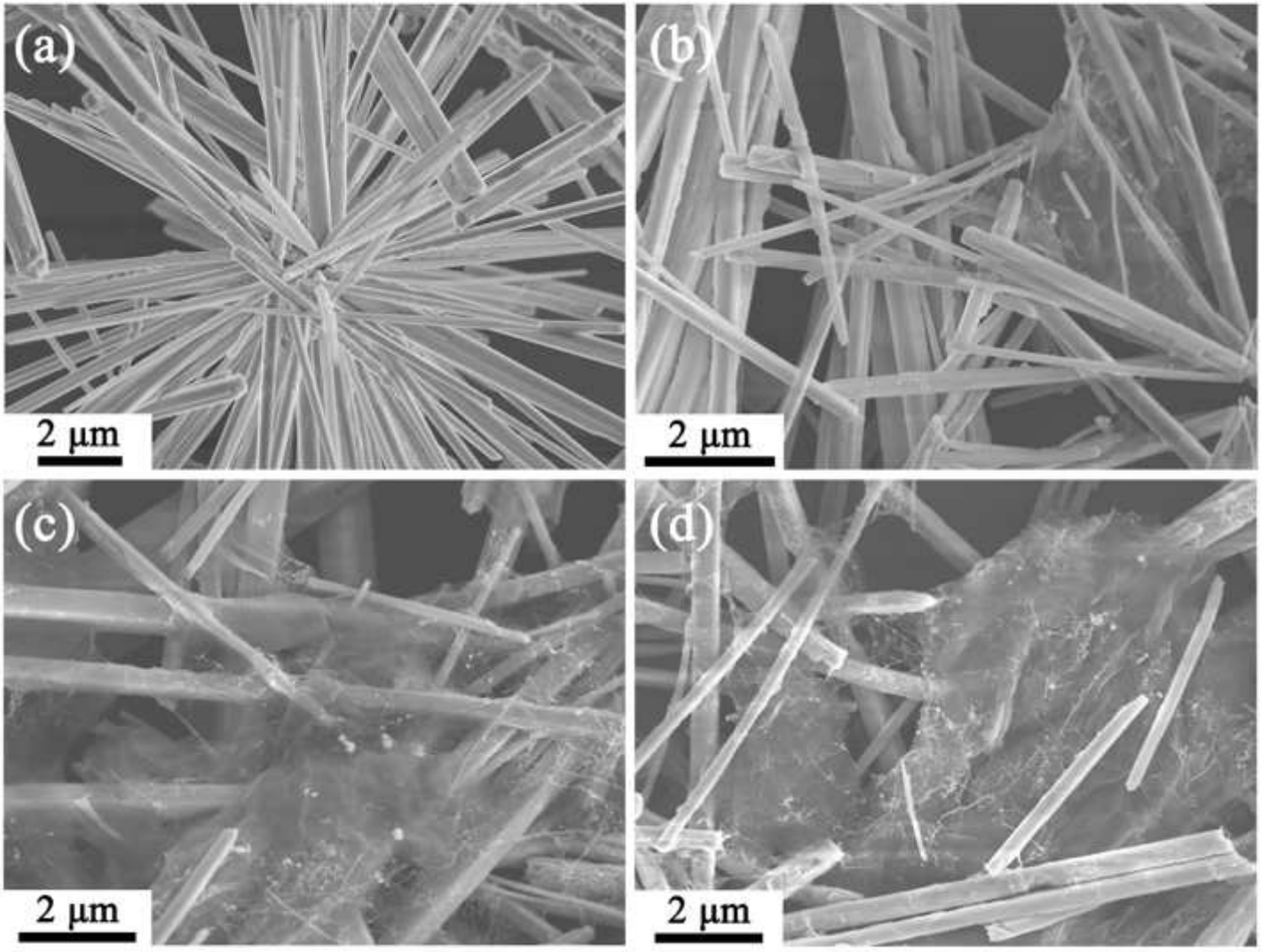

Figure 1

SEM images of the as-prepared (a) α-AgVO3, (b) 0.5 GO/α-AgVO3, (c) 1.0 GO/α-AgVO3, (d) 2.0 GO/α-AgVO3.

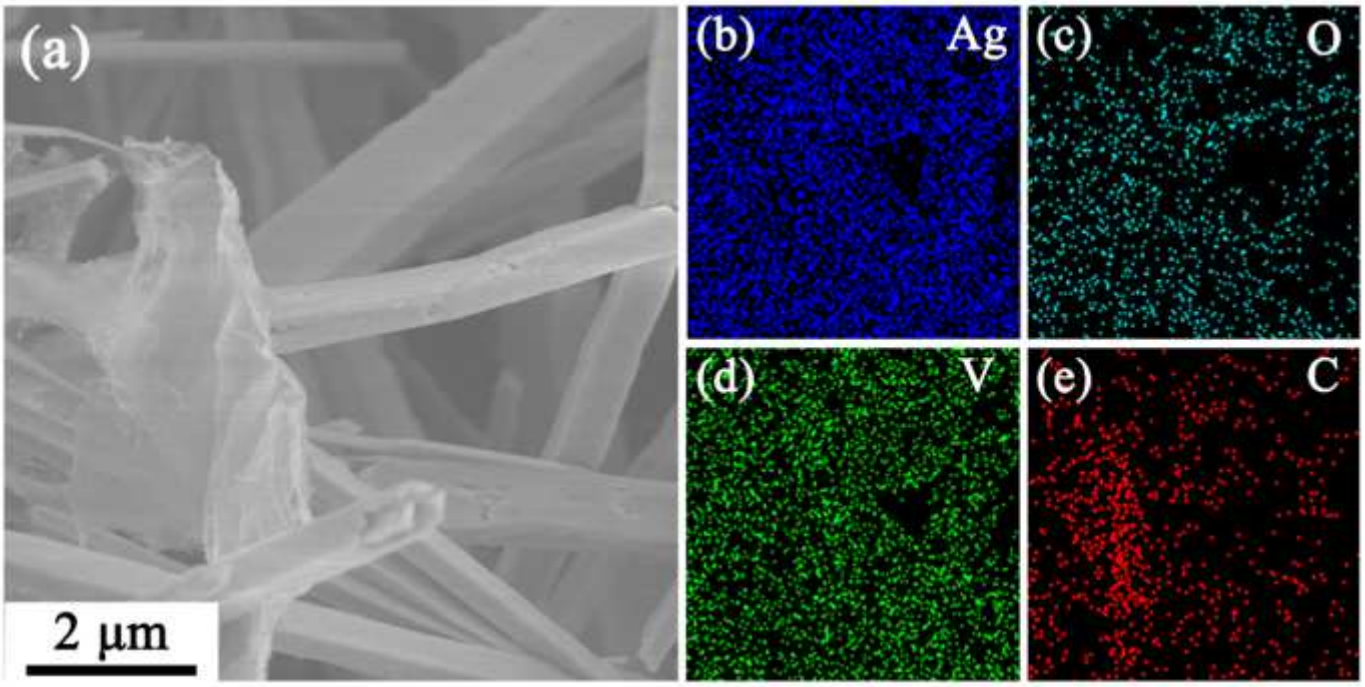

Figure 2

The SEM image of 0.5 GO/α-AgVO3 (a) and the corresponding EDS elemental mapping of (b) Ag, (c) O, (d)V, and (e) C.

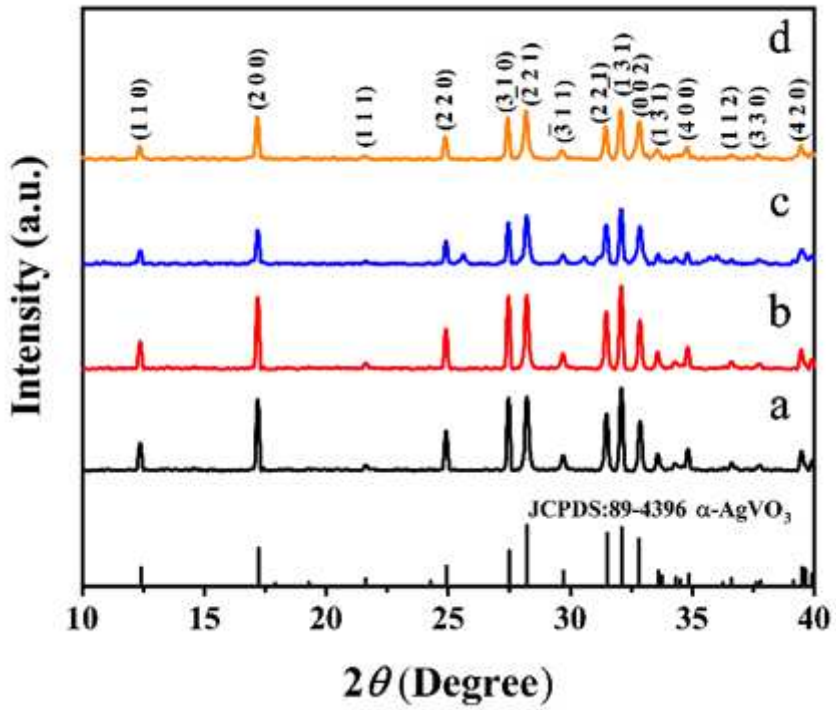

Figure 3

XRD patterns of (a) α-AgVO3, (b) 0.5 GO/α-AgVO3, (c) 1.0 GO/α-AgVO3 and (d) 2.0 GO/α-AgVO3.

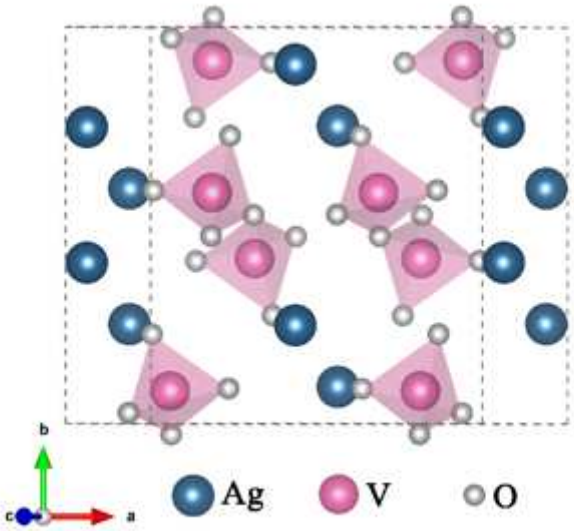

Figure 4

Crystal structure of α-AgVO3.

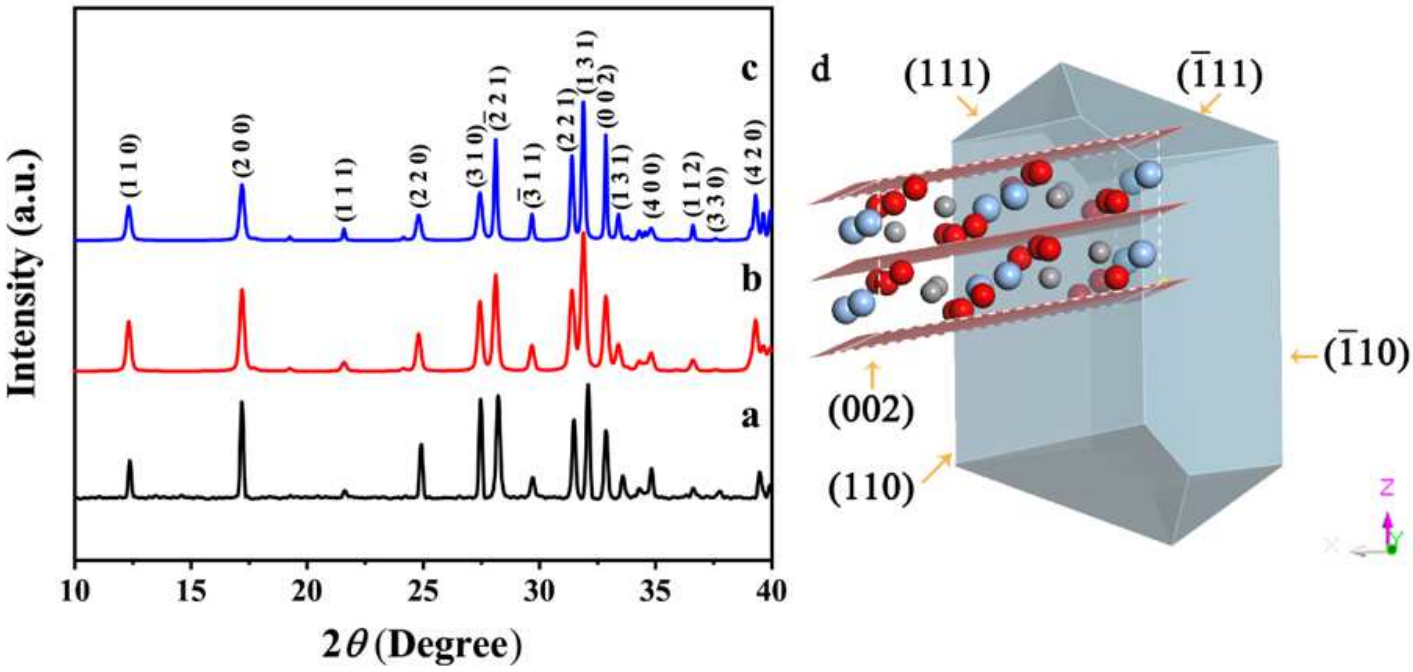

Figure 5

Experimental XRD patterns of α-AgVO3 (a), together with simulated XRD patterns of powder (b) and c-axis oriented particle (c). (d) the calculated morphology based on the theory of Donnay-Harker. (The purple crystal is the α-AgVO3 nanorod, and the plane is the (0 0 2) plane.)

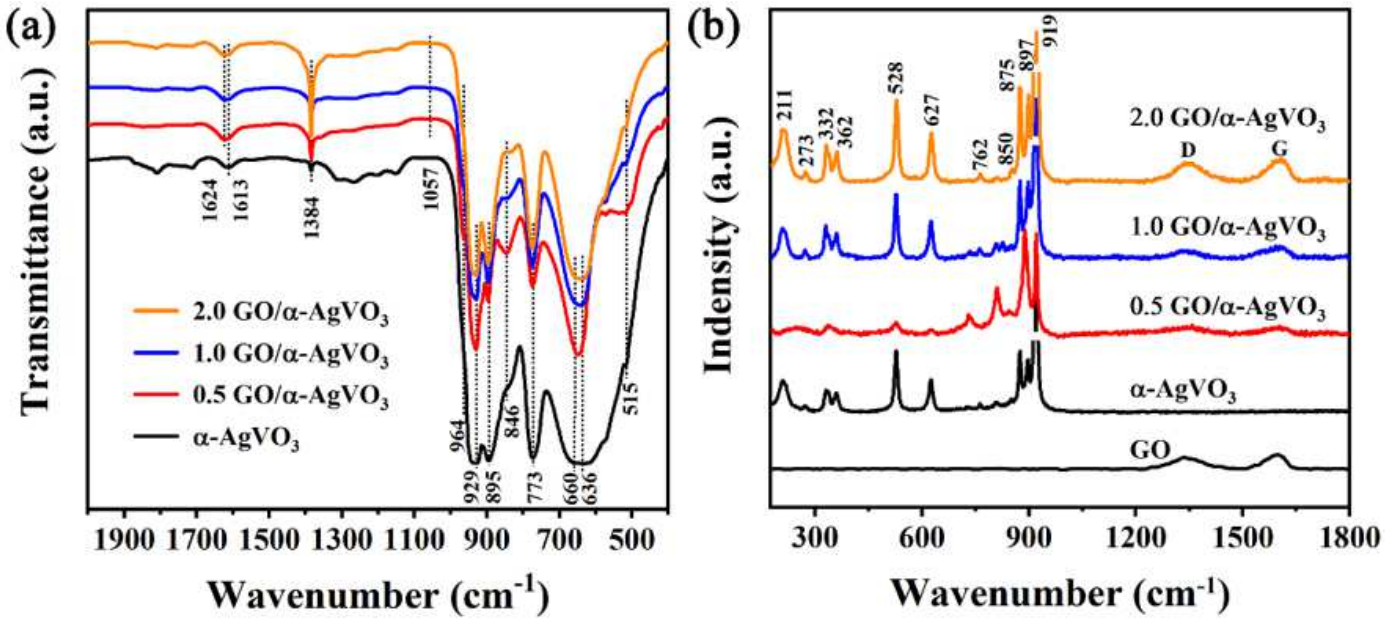

Figure 6

(a) FTIR spectra and (b) Raman spectra of α-AgVO3 and GO/α-AgVO3 with different GO contents (in 0.5 wt.%, 1.0 wt.%, and 2.0 wt.%).

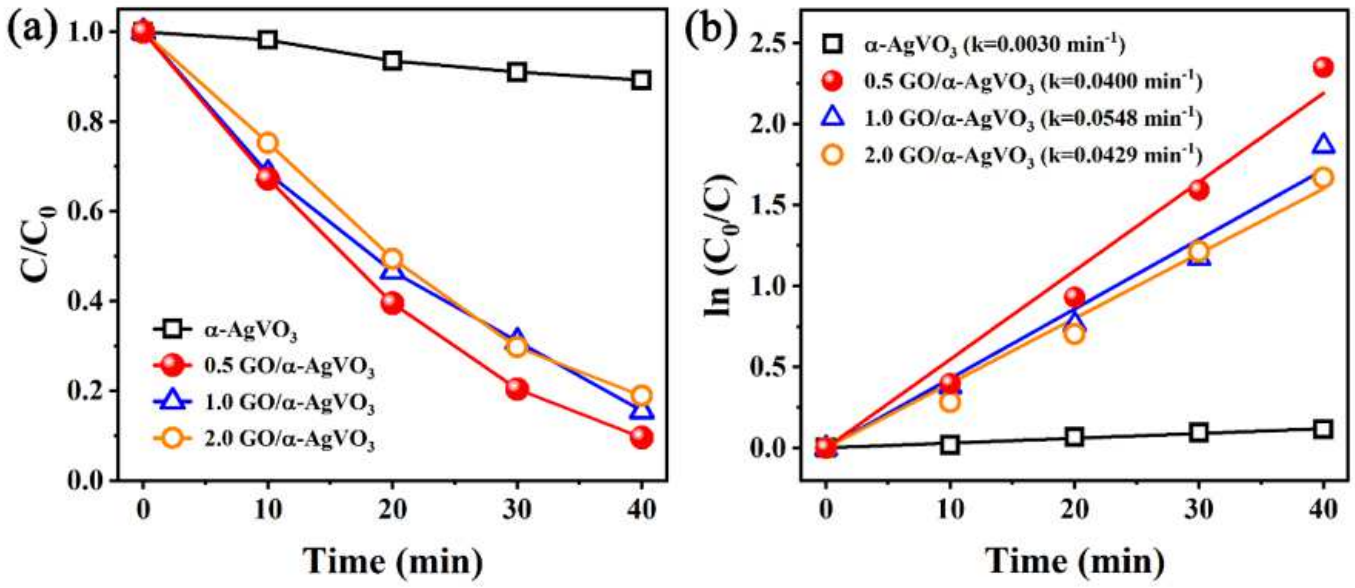

Figure 7

Photocatalytic degradation curves of RhB (a) and the corresponding pseudo-first-order kinetic curves (b).

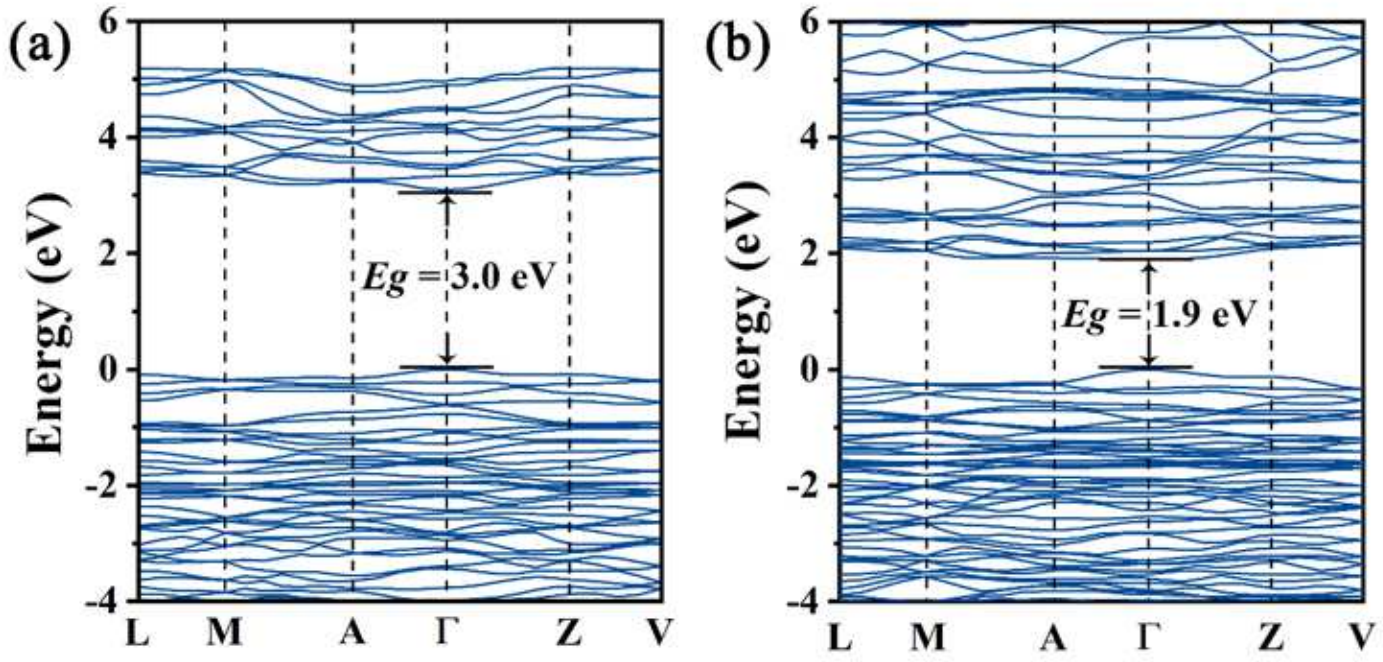

Figure 8

Band structure of α-AgVO3 along the high symmetry line in the Brillouin zone calculated by (a) GGA and (b) HSE03 functional.

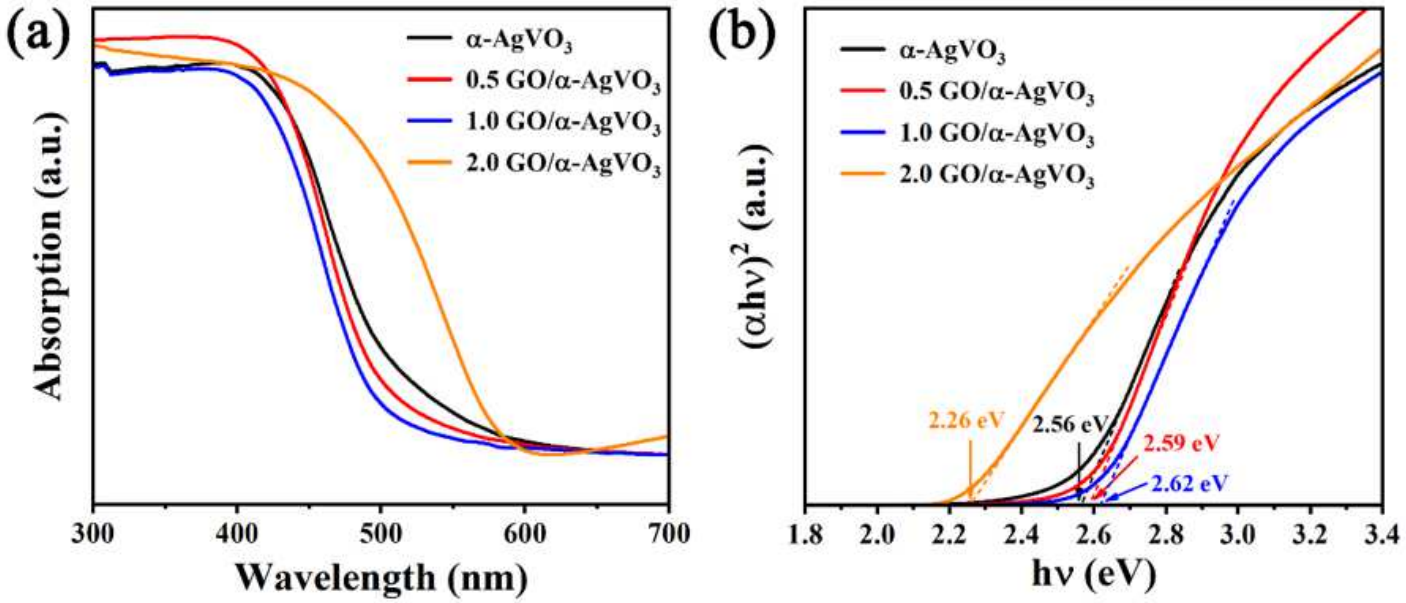

Figure 9

UV–vis diffuse reflectance spectra (a) and Kubelka–Munk plot (b) of α-AgVO3 and GO/α-AgVO3 with different GO contents (in 0.5 wt.%, 1.0 wt.%, and 2.0 wt.%).

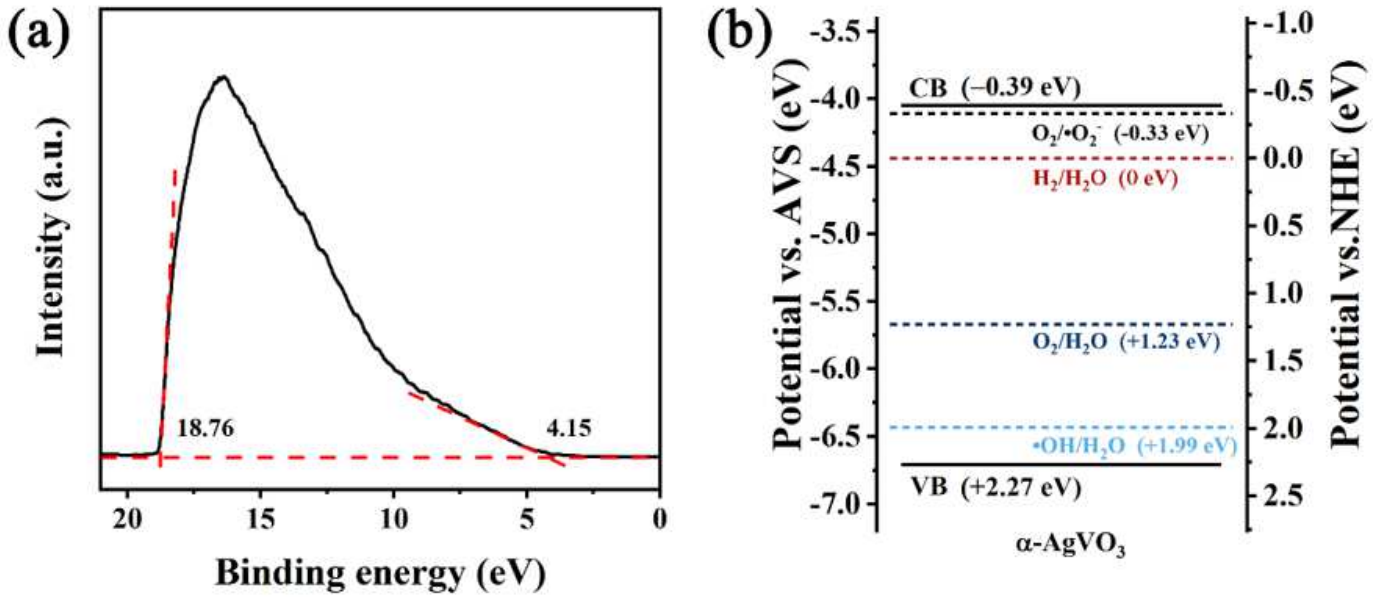

Figure 10

UPS spectra (a) and the band structure diagram of α-AgVO3(b).

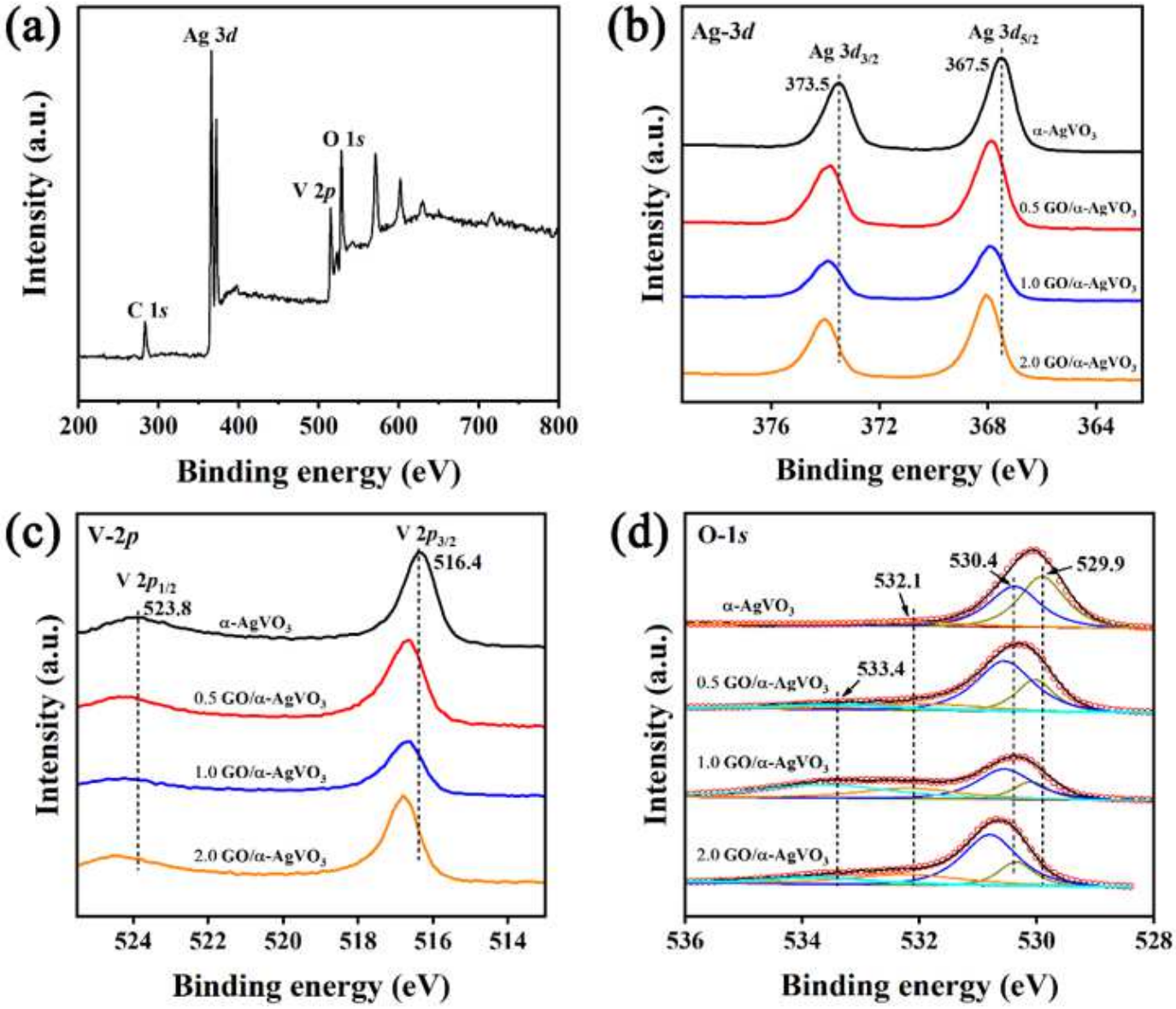

Figure 11

Full-scale XPS survey spectrum for 0.5 GO/α-AgVO3 (a) and the XPS spectra of (b) Ag 3d, (c) V 2p and O 1s for GO/α-AgVO3 with different GO contents (in 0.5 wt.%, 1.0 wt.%, and 2.0 wt.%).

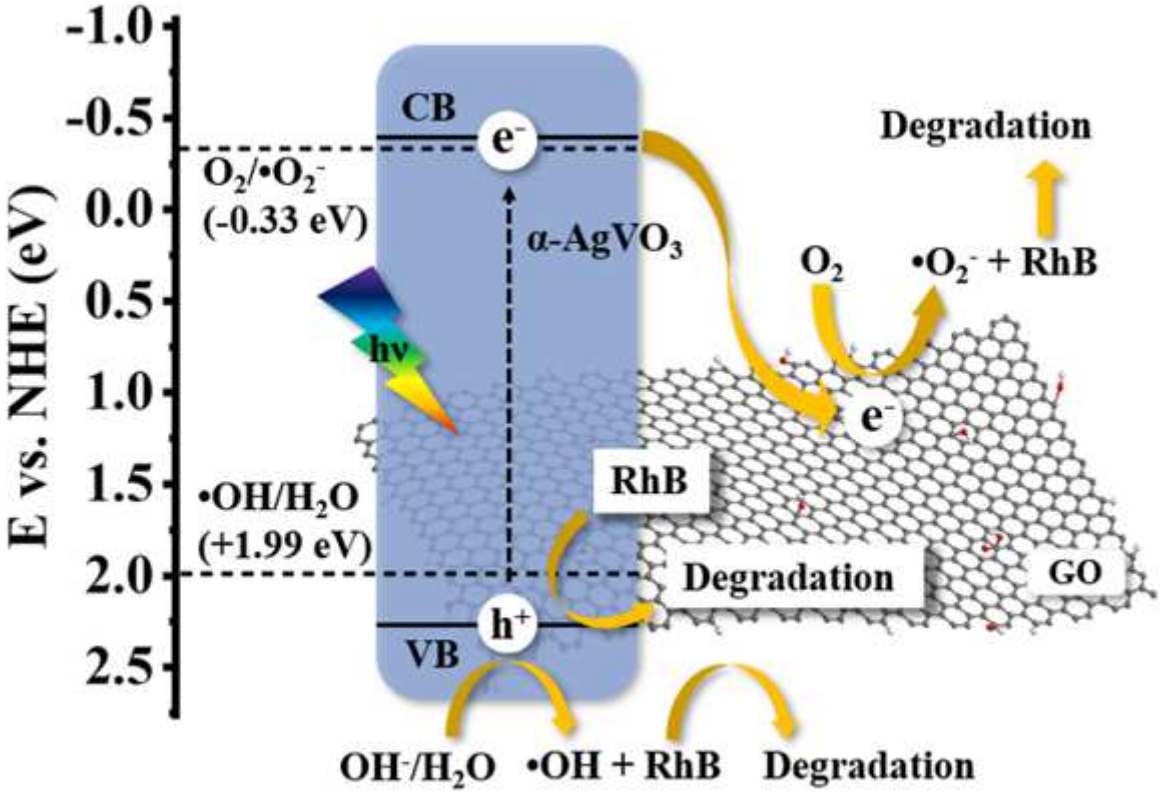

Figure 12

Proposed photocatalytic mechanism of GO/α-AgVO3 photocatalyst.